

Article

Timing of Paleozoic Metamorphism in the Jiaobei Terrane, East China: Evidence from Apatite U-Pb Age and Trace Element Composition

Kefei Sun ^{1,2}, Maoguo An ^{1,2,*}, Xiangyong Jiang ¹, Chenglong Zhi ^{1,2} and Hongjie Tan ¹¹ School of Earth Science and Resources, China University of Geosciences, Beijing 100083, China² Shandong Provincial Lunan Geology and Exploration Institute (Shandong Provincial Bureau of Geology and Mineral Resources No.2 Geological Brigade), Jining 272100, China

* Correspondence: maoguoan0311@163.com

Abstract: The northward subduction of the Paleo-Tethys oceanic crust in the Paleozoic to Mesozoic is critical for the tectonic evolution of the Qinling-Tongbai-Hong'an-Dabie-Sulu-Imjingang-Gyeonggi orogenic belt. However, the Paleozoic geological fingerprint of the Paleo-Tethys oceanic crust subduction in the Dabie-Sulu orogenic belt remains obscure. In the present study, apatite from the Muniushan monzogranite in the Houkuang area was analyzed to constrain the age of metamorphism in the Jiaobei Terrane and is regarded as the response to the Paleo-Tethys oceanic crust subduction in the Early Permian. Muniushan apatite with obvious negative Eu anomaly is enriched in LREE and depleted in HREE. The chondrite-normalized REE patterns of apatite correspond with I-type granitoids and mafic igneous rocks, implying a magmatic origin. Igneous apatite grains have reset compositional zonation in the cathodoluminescence image. Apatites plotted on a support vector machine apatite classification biplot and Eu/Y-Ce discrimination diagram shows a tendency from the region of "mafic igneous rocks and I-type granitoids" to "low and middle metamorphic". This evidence consistently suggests that the Muniushan apatite suffered metamorphism at a later stage. The twenty-six apatite grains from the Muniushan monzogranite yield a metamorphic age of 297 ± 8 Ma (by LA-ICP-MS U-Pb), which is different from the Muniushan zircon SHRIMP U-Pb results of 2110 ± 4 Ma, indicating the metamorphism occurred in the Early Permian and reset the U-Pb system of apatite. The Early Permian metamorphism that occurred in the Jiaobei Terrane is synchronous to the subduction of the Paleo-Tethys oceanic crust and is the response to the Paleo-Tethys oceanic crust subduction.

Keywords: apatite; U-Pb geochronology; trace elements; late Paleozoic metamorphism; Jiaobei Terrane

Citation: Sun, K.; An, M.; Jiang, X.; Zhi, C.; Tan, H. Timing of Paleozoic Metamorphism in the Jiaobei Terrane, East China: Evidence from Apatite U-Pb Age and Trace Element Composition. *Minerals* **2022**, *12*, 1294. <https://doi.org/10.3390/min12101294>

Academic Editors: Kunfeng Qiu, Callum Hetherington and Jan Marten Huizenga

Received: 26 August 2022

Accepted: 8 October 2022

Published: 14 October 2022

Publisher's Note: MDPI stays neutral with regard to jurisdictional claims in published maps and institutional affiliations.



Copyright: © 2022 by the authors. Licensee MDPI, Basel, Switzerland. This article is an open access article distributed under the terms and conditions of the Creative Commons Attribution (CC BY) license (<https://creativecommons.org/licenses/by/4.0/>).

1. Introduction

The Qinling-Tongbai-Hong'an-Dabie-Sulu (east-central China)-Imjingang-Gyeonggi (central Korea) orogenic belt was formed in the Paleozoic to early Mesozoic convergent plate motion (Figure 1a,b) [1–4]. The Qinling-Tongbai-Hong'an-Dabie-Sulu orogenic belt, between the North China Block (NCB) and the South China Block (SCB), experienced the early to mid-Paleozoic oceanic arc accretion, Prototethyan and Paleo-Tethys oceanic crustal subduction, the Late Permian to Triassic continental subduction, HP/UHP metamorphism and subsequent exhumation [5–10]. The arc-continent collision in the late Paleozoic was caused by the northward subduction of the Paleo-Tethys oceanic crust, leading to the low-P metamorphism in the Qinling-Tongbai orogenic belt, the HP eclogite facies metamorphism in the Hong'an orogenic belt and the crustal accretion to the NCB [11–13]. The subduction of the Paleo-Tethys oceanic crust in the Hong'an orogenic belt starts in the Carboniferous resulting in the eclogite facies metamorphism at 309 ± 3 Ma [14]. The Ogcheon belt, south of the Gyeonggi orogenic belt, is regarded as an eastern continuation of the Dabie-Sulu belt between the North and South China blocks (Figure 1a) [4,15–18]. The Ogcheon belt also underwent the Early Permian (290–280 Ma) regional metamorphic event, which is

synchronous to the Paleozoic Paleo-Tethys oceanic crust subduction [4,15,16]. However, geological fingerprints of Paleozoic arc-continent collision in the Dabie-Sulu Orogenic Belt in east China remain obscure.

The Jiaobei Terrane, northwest of the Sulu Belt, was coalesced with the Sulu Terrane during the Paleozoic to early Mesozoic convergent plate motion (Figure 1b). Paleoproterozoic Muniushan monzogranite, southeasternmost of the Jiaobei Terrane, is susceptible to the Paleo-Tethys oceanic crust subduction (Figures 1 and 2). Apatite, a common and important accessory mineral, is formed in different apatite-generation environments. The temperature sensitivity (350–570 °C) of the apatite U-Pb system makes it a representative medium-low temperature thermochronology tool [19–25]. It is prone to isotopic resetting, which occurred in the metamorphism and recorded the age of metamorphism [26–30]. In the present study, representative Muniushan monzogranite from the Jiaobei Terrane was selected to investigate a representative geological fingerprint of the Paleozoic arc-continent collision that occurred in the Dabie-Sulu orogenic belt. Muniushan apatite U-Pb geochronology and compositional analyses were conducted to prove that the late Paleozoic metamorphism that occurred in the Jiaobei Terrane was in response to the northward subduction of the Paleo-Tethys oceanic crust during the same period.

2. Geological Background

The Jiaobei Terrane, to the east of the regional Tan-Lu Fault, consists of the Jiaobei Uplift in the northwest and the Jiaolai Basin in the southeast (Figure 1a,b) [31–34]. The Jiaobei Uplift mainly comprises the Neoproterozoic Jiaodong group of amphibolites and tonalite-trondhjemite-granodiorite (TTG) gneisses and the Paleoproterozoic sedimentary Fenzishan and Jingshan groups [1,2,33,35–38]. Magmatic intrusions into the Jiaobei Uplift include the Late Jurassic (ca. 160–145 Ma) Linglong granite, the Early Cretaceous (ca. 130–122 Ma) Guojialing granitoid, and the Early Cretaceous (ca. 119–110 Ma) Aishan-Type granitoid (Figure 1b) [31,39–44]. The main controlling structure in the Jiaobei Uplift is the NE-trending Sanshandao, Jiaojia, Zhaoping, and Qixia fault zones (Figure 1b) [45–47]. The Jiaolai Basin is the Cretaceous pull-apart basin, where the development is controlled by Late Mesozoic strike-slip and pull-apart movements along NNE-trending faults [37,48–50]. The exposed formations in the area include the Paleoproterozoic sedimentary Fenzishan and Jingshan groups, the Cretaceous Laiyang group and the Cenozoic clastic rocks [51,52]. Magmatic rocks in the Jiaolai Basin comprise the Paleoproterozoic Muniushan and Early Cretaceous Aishan granites (Figure 1b) [53,54]. The main controlling structure in the Jiaolai Basin is the NE-trending Tan-Lu and Muping-Jimo fault zones (Figure 1b).

The Houkuang area is located in the northeastern part of the Jiaolai Basin (Figures 1 and 2). Abundant gold resources in the area are widespread, such as the Tudui, Shawang, Dongliujia, Longkou, and Houkuang gold deposits [34,43,55,56]. The strata consist of the Paleoproterozoic biotite granulite, diopside granulite and biotite schist, Cretaceous gravel sandstone, muddy siltstone and conglomerate, and Cenozoic clastic rocks. The major fault is dominated by the SE-dipping Guocheng Fault. The main magmatic rock exposed in the area is the Paleoproterozoic Muniushan monzogranite (Figure 2).

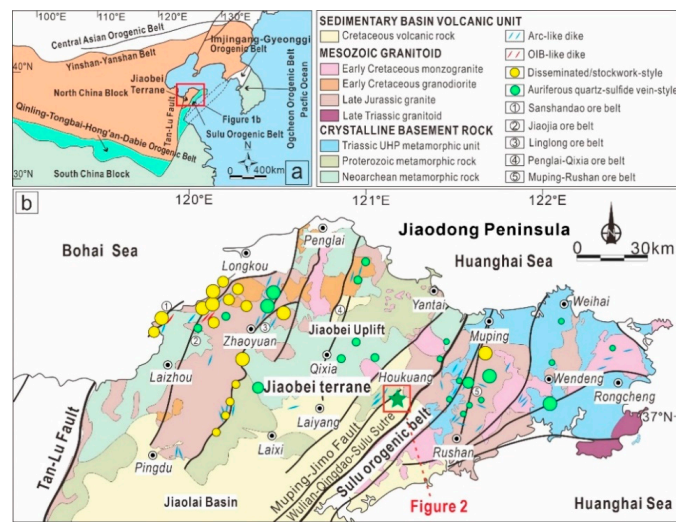


Figure 1. Simplified map showing the location of the Jiaobei Terrane (a) and geological map of the Jiaodong Peninsula (b). The dashed line means the eastern continuation of the Dabie-Sulu orogenic belt and the rectangle shows the Muniushan monzogranite [35].

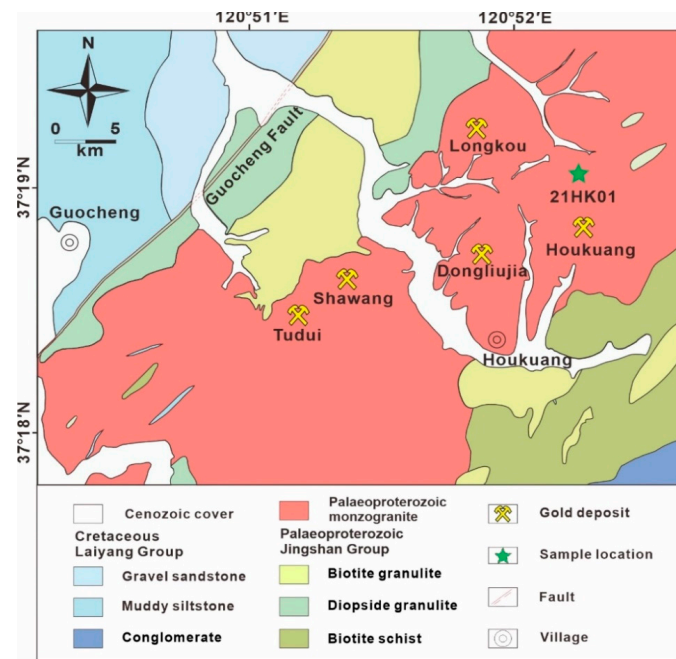


Figure 2. Geological map of the Houkuang gold deposit in the Jiaolai Basin showing the major geological units and sample locations [35].

3. Samples and Methodology

3.1. Sample Description

One monzogranite sample was collected from the Muniushan pluton, namely 21HK01 (37°19'01" N, 120°51'58" E). The sample locations and hand specimen photographs are shown in Figures 2 and 3. Monzogranite intrudes into the Paleoproterozoic Jingshan group (Figure 3a,b). Shear joints are distributed on the surface of Muniushan pluton, which was affected by the mylonitization (Figure 3c,d). The light gray-black monzogranite samples are characterized by a medium-fine granular texture and massive structure (Figure 4a). The main minerals are quartz, plagioclase, and K-feldspar, and the secondary minerals are chlorite and sericite (Figure 4b,c). The quartz from monzogranites is subhedral to anhedral and the particle size distribution ranges from 0.1~0.6 mm (Figure 4b). The plagioclase

and K-feldspar have subhedral to anhedral crystals, of which the particle size distribution ranges from 0.2 to 0.5 mm and 0.1 to 0.3 mm (Figure 4b,c). Chloritization and sericitization were observed under the microscope (Figure 4b,c). The apatite is mainly accessory mineral in the monzogranite (Figure 4d).

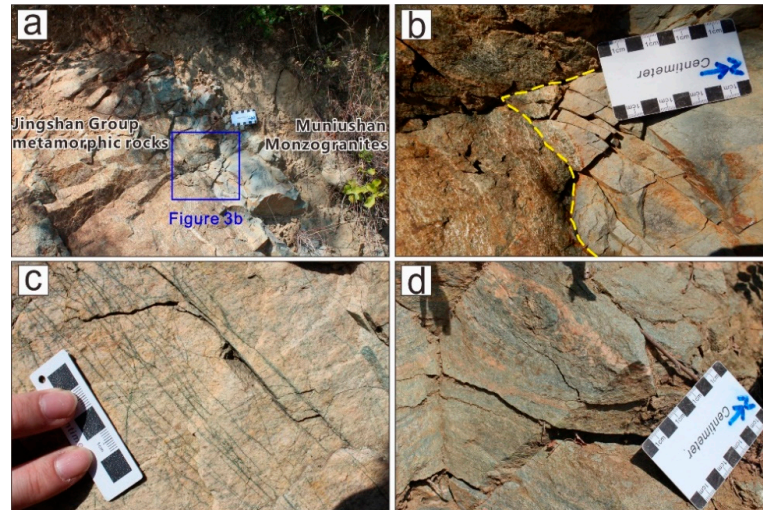


Figure 3. Field photographs of the Muniushan monzogranites. Field photographs showing the Monzogranite intrudes into the Paleoproterozoic Jingshan group (a,b). Field photographs showing the shear joint and mylonitization on the monzogranite (c,d).

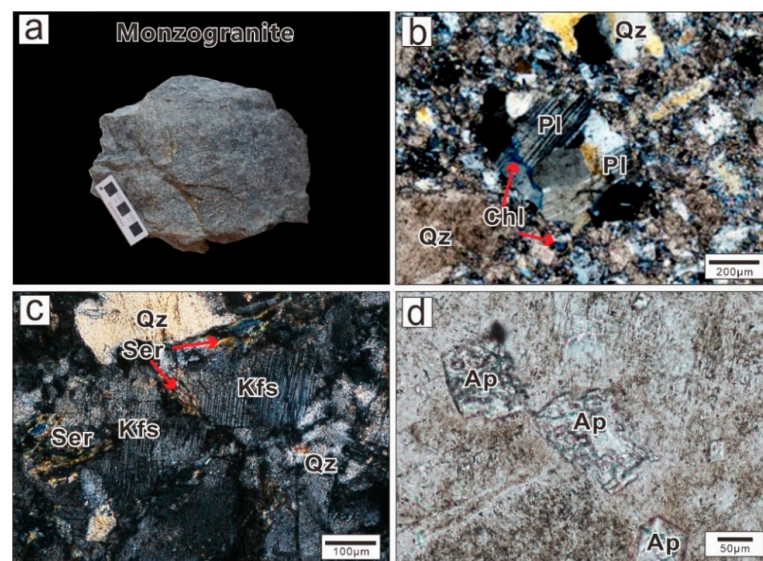


Figure 4. Photomicrographs showing the Muniushan monzogranite samples. Hand specimens of the Paleoproterozoic Muniushan monzogranites (a). Transmitted crosspolarized light photomicrographs (b,c). Single polarized photomicrograph (d). Pl = plagioclase, Qz = quartz, Chl = chlorite, Kfs = K-feldspar, Ser = sericite, Ap = apatite [23,24,57].

3.2. Apatite LA-ICP-MS U-Pb Dating

The separation of apatite grains was carried out at the Langfang Chengxin Geological Service Co., Hebei Province, China. The apatite grains were separated from the Muniushan monzogranite through coarse and fine crushing, panning, magnetic separation, and other methods. Magnetic techniques were used to separate the apatite grains from the clastic grains. In order to investigate the internal structure of the apatite, the relatively complete and transparent apatite crystals were mounted in the epoxy, polished to nearly half-section,

and cleaned in an ultrasonic cleaner containing a 5% HNO₃ solution. Transmission, reflection, and CL imaging were also completed at the Langfang Chengxin Geological Service Co., Langfang, China.

The apatite U-Pb analyses were carried out using the LA-ICP-MS at the Yanduzhongshi Geological Analysis Laboratory, Beijing, China. The laser analyses were performed using a Neptune double-focusing multiple-collector ICP-MS attached to a 193 nm NWR193 Ar-F excimer laser ablation system. All apatite analyses were completed with a beam diameter of 37 µm, 10 Hz repetition rate and a 0.25 mJ/pulse power, during a 70 s analysis including 20 s measurement of gas blank, followed by ablation of the sample for approximately 40 s by raster. MAD2 [58], McClure Mt. [59], Otter Lake and Durango were used as the age standards for apatite U-Pb. Data were processed using the Isoplot 3.0 program [21,60,61].

3.3. Trace Element Analyses of Apatite

The LA-ICP-MS analyses of trace elements in apatite were carried out at the Isotopic Laboratory, Tianjin Center, China Geological Survey, Tianjin, China, using a 193 nm excimer ArF LA system and an Agilent 7900a ICP-MS. All analyses were conducted with a beam diameter of 29 µm, 8 Hz ablation frequency, and 80 mJ laser energy. In order to ensure the accuracy of the test, the NIST SRM 610 and 612 reference material glasses were used as an external reference material for trace element determinations on apatite. The internal element standard isotope was ⁴³Ca for apatite trace element analyses. Concordia plots and age calculations were reported at the 2σ uncertainty level and were processed using the ICPMSDataCal 11.8 program [62]. Thirty-three elements such as Ca, P, Si, Al, Fe, Mg, Mn, Sr, Y, and REE of apatite were determined in the experiment.

4. Results

4.1. Morphology and Geochronology of Apatite

The 21HK01 apatite was dated by LA-ICP-MS, and the morphology and plots of data are shown in Table 1 and Figure 5b,c. Most apatite grains from the monzogranite (21HK01) are colorless, transparent, and subhedral to anhedral. Apatite grains from sample 21HK01 display lengths of 100–250 µm and length/width ratios ranging from 2:1 to 4:1. In the CL image, apatite grains show a changed compositional zonation. Twenty-six apatite grains were analyzed on the light and dark compositional zonation. The samples yield a lower intercept age of 297 ± 8 Ma (n = 26, MSWD = 1.2) and a weighted mean age of 295 ± 11 Ma (n = 26, MSWD = 0.7) (Figure 5b,c), representing the metamorphic age.

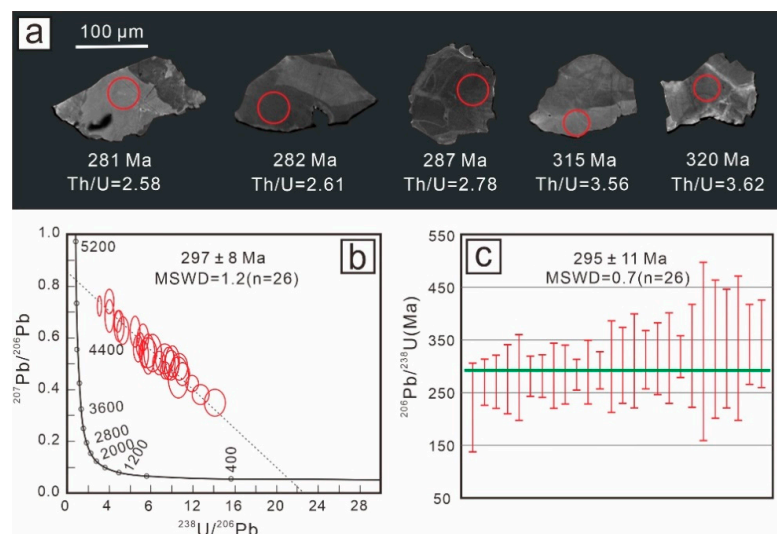


Figure 5. CL image of apatite grains from monzogranite sample 21HK01 (a). Apatite Tera-Wasserburg concordia plots for Muniushan apatite U-Pb analyses (b). Weighted mean ²⁰⁶Pb/²³⁸U ages for Muniushan apatite U-Pb analyses (c).

4.2. Trace Elements of Apatites

The trace element composition and plot of apatite are shown in Table 2 and Figure 6. The total LREE (Σ LREE) ranges from 650 to 1591 ppm, and the total HREE (Σ HREE) ranges from 231 to 855 ppm. The Eu anomalies are >0.62 ($Eu/Eu^* = 0.62-1.02$). Apatite is enriched in LREE and depleted in HREE. The contents of Sr and Y from the Muniushan apatite ranges from 440.8 to 655.6 ppm and 128.4 to 503.4 ppm. The Sr/Y contents are between 1.24 and 4.43.

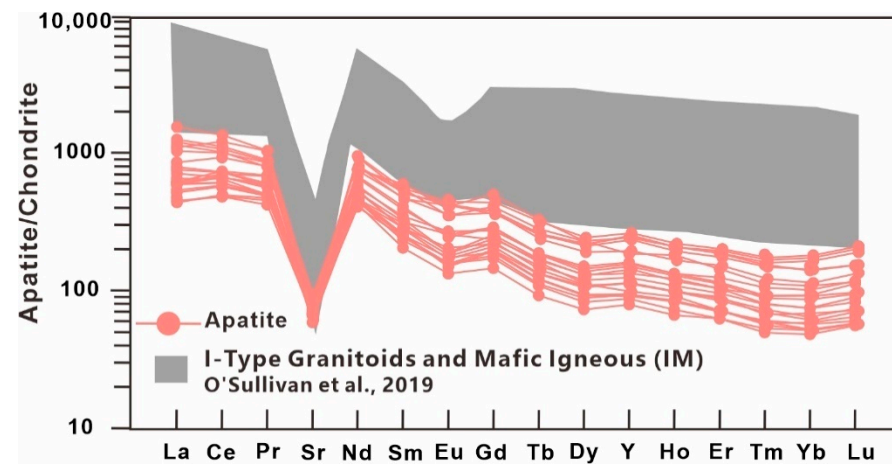


Figure 6. Chondrite-normalized REE + Sr multi-element plots ('spidergrams') of Muniushan apatite [63].

Table 1. LA-ICP-MS U-Pb apatite data from monzogranite (21HK01) at Houkuang.

Sample No.	Th	U	Th/U	Isotopic Ratios					
				$^{207}\text{Pb}/^{206}\text{Pb}$		$^{207}\text{Pb}/^{235}\text{U}$		$^{206}\text{Pb}/^{238}\text{U}$	
				Ratio	1 σ	Ratio	1 σ	Ratio	1 σ
Apatite from monzogranite (21HK01): 297 ± 8 Ma (MSWD = 1.3, n = 26)									
21HK01-02	18	5	3.56	0.7492	0.0190	25.2888	1.2111	0.2488	0.0110
21HK01-03	13	4	3.61	0.5126	0.0203	6.2460	0.2403	0.0935	0.0028
21HK01-04	11	3	3.62	0.5533	0.0239	6.9290	0.2295	0.0995	0.0027
21HK01-05	16	6	2.78	0.6071	0.0208	11.4069	0.4121	0.1383	0.0042
21HK01-07	6	3	2.26	0.6596	0.0245	13.1914	0.4346	0.1541	0.0045
21HK01-08	21	4	4.68	0.3804	0.0208	3.3962	0.1559	0.0709	0.0021
21HK01-09	13	5	2.47	0.4698	0.0178	5.7372	0.2228	0.0909	0.0024
21HK01-11	8	4	2.00	0.5315	0.0229	7.6438	0.3909	0.1073	0.0043
21HK01-15	15	5	3.15	0.5119	0.0234	6.7918	0.2511	0.1003	0.0029
21HK01-17	15	6	2.56	0.4387	0.0131	4.8747	0.1352	0.0840	0.0018
21HK01-18	10	4	2.38	0.5298	0.0257	7.0921	0.2743	0.1036	0.0027
21HK01-19	13	4	3.21	0.3997	0.0159	4.0936	0.1495	0.0785	0.0021
21HK01-20	7	3	2.07	0.5729	0.0290	9.1053	0.4528	0.1223	0.0051
21HK01-22	12	3	3.73	0.5013	0.0322	5.7695	0.2848	0.0942	0.0035
21HK01-23	7	3	2.15	0.6555	0.0166	18.8423	0.7507	0.2071	0.0062
21HK01-24	8	3	2.34	0.5269	0.0181	7.8596	0.2612	0.1137	0.0033
21HK01-25	10	5	2.09	0.5818	0.0185	11.2593	0.3663	0.1431	0.0033
21HK01-26	9	3	2.73	0.5499	0.0235	9.6934	0.6076	0.1298	0.0058
21HK01-27	14	5	2.61	0.4891	0.0130	6.9329	0.1698	0.1067	0.0022
21HK01-29	6	3	2.30	0.5879	0.0313	9.5268	0.2753	0.1290	0.0042
21HK01-30	9	3	2.58	0.6800	0.0257	23.3600	1.2905	0.2484	0.0102
21HK01-32	7	3	2.33	0.6587	0.0244	17.7866	0.7779	0.2014	0.0080
21HK01-33	10	3	2.94	0.6387	0.0213	16.1999	0.7132	0.1882	0.0080
21HK01-34	14	4	3.28	0.7293	0.0158	32.4341	0.9251	0.3267	0.0085
21HK01-36	5	3	1.75	0.5571	0.0205	10.0301	0.2563	0.1366	0.0030
21HK01-37	7	3	2.46	0.5858	0.0206	11.2902	0.3714	0.1475	0.0040

Table 2. LA-ICP-MS apatite trace element composition.

Sample	01-01	01-02	01-06	01-07	01-12	01-13	01-14	01-18	01-19	01-21	01-23	01-24	01-26	01-28	01-29
P	186,406	185,857	186,152	190,362	183,815	183,180	201,961	221,295	201,068	195,086	182,191	178,812	184,656	187,632	187,714
Sr	614.5	495.8	518.2	503.8	613.6	622.6	607.5	655.6	503.3	440.8	504.5	539.7	551.5	518.9	511.2
Y	141.8	185.4	393.6	253.1	151	503.4	202.1	148	216.2	243	182.3	152.7	128.4	260	300.8
La	125.7	109	268	150.4	148.4	116.1	184.8	144.1	146.1	143	151	131.4	159.6	193.6	209
Ce	359.4	304.3	762.9	465.1	381.9	356.6	459.1	384.1	417.3	448.4	422.3	367.1	409.1	459.7	585.1
Pr	47.7	41.3	101.3	67.5	49.5	61.1	56.6	48.2	58.6	66.2	56.3	48.4	48.7	59	78.5
Nd	214.5	195.9	458.8	317.2	218.9	363.3	252.7	214.3	280.1	327.9	258.7	226.4	204.2	270	366.5
Sm	36.8	38.9	87.3	61.6	39.1	123.4	45.2	40	52.5	64.7	44.4	40.7	32.4	54.8	94.1
Eu	9.4	9.4	21	15.2	9.5	27.4	12.2	10.4	11.3	14.7	10.1	8.9	8	16.2	24.5
Gd	36.4	41.9	86.4	61.2	38.2	148.7	46.5	40.1	53.9	60.7	44.3	41.2	30.9	58	106.2
Tb	4.2	5.1	10.9	7.2	4.3	19.3	5.9	4.7	6.6	7.1	5.2	4.7	3.6	7.2	12.7
Dy	21.7	27.6	59.9	37.7	23.2	91.1	31.3	24.2	34.2	36.2	28.4	24.6	19.1	39.4	60.1
Ho	4.2	5.8	12.3	7.8	4.8	16.6	6.4	4.9	7.1	7.5	5.8	4.9	3.9	7.8	10.6
Er	10.7	15	31.9	19.6	12	40.3	16.4	12.3	17.7	19.1	15.4	12.3	10.7	21.3	24.6
Tm	1.4	1.9	4.1	2.4	1.6	4.8	2.1	1.5	2.1	2.3	1.8	1.6	1.3	2.8	3
Yb	9.1	11.3	24.6	16.3	10	26.6	13.2	10.3	13.1	15.1	12	9.2	8.4	17.8	19
Lu	1.5	1.9	4	3	1.6	3.9	2.3	1.7	2.2	2.5	1.9	1.5	1.5	3.1	3
Sr/Y	4.33	2.67	1.32	1.99	4.06	1.24	3.01	4.43	2.33	1.81	2.77	3.53	4.29	2	1.7
ΣLREE	747	650	1591	1000	799	897	953	791	902	985	888	773	822	982	1239
ΣHREE	231	296	628	408	247	855	326	248	353	394	297	253	208	417	540

5. Discussion

5.1. Origins of Apatite

Apatites in this study are subhedral to anhedral and show pronounced LREE enrichment and HREE depletion on their chondrite-normalized REE patterns (Figures 5a and 6). As seen in the CL images, apatite grains show a changed but homogeneous compositional zonation (with light-dark zoning) (Figure 5a) and are interpreted to be of primary magmatic origin [64,65]. The “coupled REE pattern” of Muniushan apatite also shows the similar curve of apatite in mafic igneous rocks and I-type granitoids previously published, supporting the view of magmatic origin (Figure 6) [65–71]. In addition, the support vector machine apatite classification biplot and Eu/Y-Ce discrimination diagram show that Muniushan apatite has a trend toward the low- and medium-grade metamorphic and metasomatic fields that is interpreted as the influence of metamorphism at a later stage (Figure 7) [3,24,72,73]. The apatite only appears in Muniushan monzogranite, which implies that the apatite has a genetic relationship with the monzogranite. Previous studies of the geochronological data of Muniushan monzogranite show emplacement ages of ca. 2.1 Ga and metamorphic ages of ca. 1.85 Ga [74–77]. The apatite yields a U-Pb Tera-Wasserburg concordia plot with lower intercept age of 297 ± 8 Ma, which is significantly different from the zircon SHRIMP U-Pb geochronology results of the Muniushan monzogranite cluster at 2110 ± 4 Ma [77]. This may be explained by the closure temperature, at which the rock is formed and cools to a temperature where the loss path of daughter isotopes is negligible compared to the accumulation amount after radioactive timing begins [73,78]. The temperature of medium-grade metamorphism is above 550 °C, which is often higher than the apatite U-Pb closure temperature of 350–550 °C, and is easily to lead the isotopic resetting [3,79–82]. Therefore, we present Muniushan apatite with a magmatic origin that is affected by the metamorphism later.

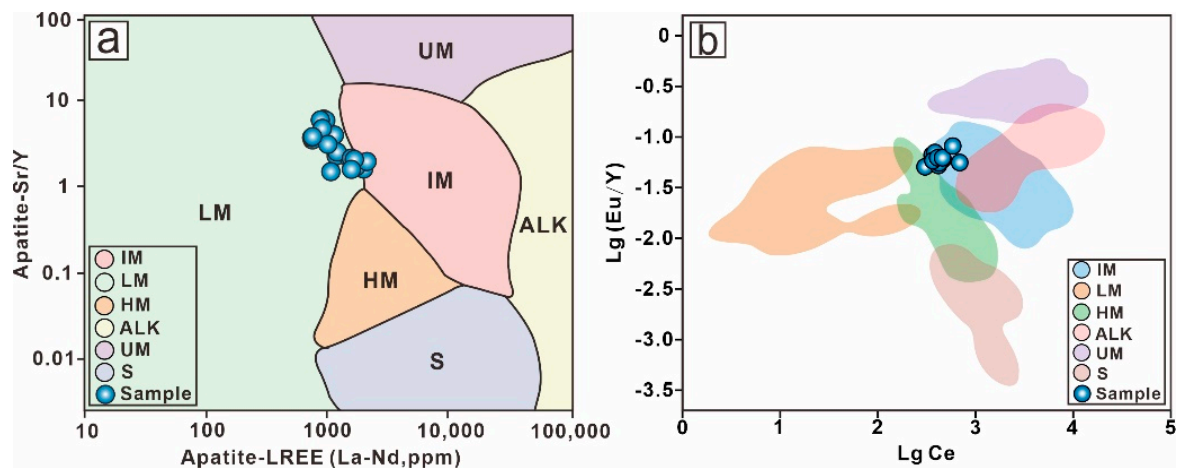


Figure 7. Diagrams showing apatite trace element composition. Apatites plotted on a support vector machine apatite classification biplot (a) and a Eu/Y vs. Ce discrimination diagram of apatite [83,84] (b). Abbreviations: ALK—alkali-rich igneous rocks; HM—partial melts/leucosomes/high-grade metamorphic rocks; IM—mafic I-type granitoids and mafic igneous rocks; LM—low- and medium-grade metamorphic and metasomatic rocks; S—S-type granitoids and high aluminum saturation index (ASI) ‘felsic’ I-types; UM—ultramafic rocks including carbonatites, lherzolites, and pyroxenites.

5.2. Implications of the Timing of Paleozoic Metamorphism in the Jiaobei Terrane

The metamorphism of Muniushan apatite may be caused by the hydrothermal fluid from the magmatic intrusion event that occurred in the Early Permian. The apatite U-Pb age of 297 ± 8 Ma from the monzogranite samples represents the age of the magma intrusion. However, no magmatic hydrothermal events have been reported in the late Paleozoic in the Jiaobei Terrane so far. Geological fingerprints of the Paleozoic magmatic intrusion are also lacking in the Jiaobei Terrane to prove this [33–35,45,48]. Therefore, we suggest that the metamorphic age of Muniushan apatite may be explained by the northward subduction of the Paleo-Tethys oceanic crust. In the Carboniferous to early Mesozoic, the Paleo-Tethys oceanic crust subducted northward, and the Qinling-Tongbai-Hong’an-Dabie-Sulu (east-central China)-Imjingang-Gyeonggi (central Korea) orogenic belt was influenced by the subduction [85–93]. Thus, we propose that metamorphism of Muniushan apatite may be affected by the northward subduction of the Paleo-Tethys oceanic crust and is the response of the Jiaobei Terrane to the subduction event. Apatite’s U-Pb age of 297 ± 8 Ma represents the age of the Early Permian subduction.

Previous studies along the Qinling-Tongbai-Hong’an-Dabie-Sulu collisional belt show that the Hong’an-Dabie-Sulu collisional belt was influenced by the subduction of the Paleo-Tethys oceanic crust in the Permo-Triassic [2,17,88,94,95]. The Hong’an Block situated in the west of the Dabie-Sulu orogenic belt forms the transition between zones exposing low-pressure and ultra-high-pressure rocks and is a coherent part of the Triassic Dabie-Sulu HP-UHP Terranes [88,89]. The subduction of the Paleo-Tethys oceanic crust possibly starts at ca. 320–300 Ma, as suggested by the late Paleozoic eclogite facies metamorphism in the Huwan shear zone in the Hong’an Block [2]. Published Nd isotope studies for eclogites in the Huwan shear zone have shown that eclogites have high $Nd_{(t)}$ values of -1.9 to 5.8 , indicating the protoliths were derived from oceanic basalts [96]. Previous zircon Hf isotope analyses from the eclogite in the Huwan shear zone exhibit a large range in $\epsilon Hf_{(t)}$ values from -4.9 to 12.4 and young T_{DM} age of 516 ± 48 Ma and are interpreted as the incorporation of a small quantity of older crustal materials during the protolith formation [1]. All these studies, therefore, argue for an eclogite connection of the Late Silurian. Metamorphic zircons from the eclogite in the Huwan shear zone are characterized by relatively flat REE patterns, low $^{176}Lu/^{177}Hf$ ratios (0.000004 – 0.000075) and slightly negative Eu anomalies ($Eu/Eu^* = 0.31$ – 1.02) [2]. The early crystallization of plagioclase would reduce the Eu contents in residual melts and then influence their concentrations in zircon crystallizing

from such magma [64]. Thus, it is considered that zircon was formed under eclogite facies conditions, in the presence of garnet and absence of feldspar [2]. Published ^{40}Ar - ^{39}Ar , U-Pb, Rb-Sr, and Sm-Nd ages to date the eclogite facies metamorphism in the Hong'an Block span from ca. 420–220 Ma [1,13,14,97–99]. According to the in situ zircon U-Pb and mineral Lu-Hf isochron methods, the Carboniferous metamorphic ages were documented from the same samples in several outcrops from the Huwan shear zone [94,95,97,98]. The Carboniferous zircon U-Pb ages range from 315 ± 17 to 301 ± 13 Ma with a weighted mean of 309 ± 3 Ma, which is taken as the best estimated age of the eclogite facies metamorphism, starting in the Huwan shear zone [2,14]. In addition, previous simultaneous in situ trace element and Lu-Hf and U-Pb isotope analyses of zircon grains from the Xiong'dian and Sujiahe eclogite in the Hong'an Block identify that the eclogite facies metamorphism occurred persistently in the Late Carboniferous to Early Permian period at ca. 306 to 283 Ma [90,91,100]. Taken together, these dates provide unambiguous evidence for the Carboniferous eclogite facies metamorphism. Previously, it has been suggested that the oceanic and continental subductions were a continuous process in the Hong'an orogenic belt, and the subduction of Paleo-Tethys oceanic crust began prior to ca. 315 Ma, reaching peak HP eclogite facies metamorphism at ca. 310 Ma, and starting exhumation at ca. 260 Ma [95]. Thus, the eclogite facies metamorphism in the Carboniferous in the Huwan shear zone is regarded as the response to the Paleo-Tethys oceanic crust subduction. Similar evidence was also found in the Ogcheon belt in South Korea [4,15,16,101]. The Ogcheon belt (south of the Gyeonggi belt), located in the east of the Dabie-Sulu orogenic belt, is often seen as the eastern continuation of the Dabie-Sulu orogenic belt [4,92]. According to the Pb-Pb whole-rock ages of slate and uraninite electron-microprobe Th-U total Pb chemical ages, the Ogcheon belt underwent the Early Permian (290–280 Ma) regional metamorphic event that was synchronous to the Paleozoic Paleo-Tethys oceanic crust subduction [4,15,16,101]. This study supplied the Early Permian metamorphic ages that are consistent with the Hong'an Block and Ogcheon belt and are recorded by the Muniushan apatite in the Jiaobei Terrane.

The late Paleozoic has been recognized as a quiet period for the Jiaobei Terrane due to the lack of Paleozoic geological fingerprints that record relevant geological information. However, detrital zircon of the Early Permian age (280 Ma) with metamorphic genetic characteristics was found in the Linsishan Formation in the Jiaolai Basin, indicating the Jiaobei Terrane may have experienced the metamorphism during the Early Permian at ca. 280 Ma [102]. The stratum of the Linsishan Formation consists of conglomerate and microconglomerate, which have the properties of nearby depositions, implying the source of metamorphic zircon is Jiaobei Terrane [103,104]. The Muniushan apatite in this study yields the Early Permian metamorphic age (297 ± 8 Ma) that is compatible with the metamorphic zircon (280 Ma) and thus is interpreted as the occurrence of the Early Permian metamorphism in the Jiaobei Terrane. The Jiaobei Terrane was in a stable uplift and denudation stage in the late Paleozoic. Here, we argue that the Early Permian metamorphism in the Jiaobei Terrane may be caused by the northward subduction of the Paleo-Tethys oceanic crust, and the geochronological result of the Hong'an Block and Ogcheon belts is an important response to the Paleo-Tethys oceanic crust subduction, which supports this point. In summary, this research proves the occurrence of the Early Permian metamorphism in the Jiaobei Terrane, which is synchronous to the northward subduction of the Paleo-Tethys oceanic crust and may be the response to the subduction.

6. Conclusions

1. The origin of the Muniushan apatite is magmatic, the compositional characteristics being similar to the apatite in mafic igneous rocks and I-type granitoids previously published. Apatite was formed simultaneously with the Paleoproterozoic Muniushan monzogranite but suffered metamorphism later.
2. The combination of the composition and U-Pb ages of apatite can be used to constrain the younger metamorphic event that occurred in the Jiaobei Terrane in the Early Permian. Uranium-Pb geochronology of the Muniushan apatite gives a metamorphic

age of 297 ± 8 Ma, consistent with the metamorphic ages in the Hong'an Block and Ogcheon belt which represent the response of the Jiaobei Terrane to the Paleo-Tethys oceanic crust subduction in the Early Permian.

Author Contributions: Conceptualization, M.A.; writing, K.S.; review and editing, C.Z. and X.J.; formal analysis, C.Z. and H.T. All authors have read and agreed to the published version of the manuscript.

Funding: This research was funded by the National Natural Science Foundation of China (42130801), the Open Funding of Shandong Provincial Lunan Geology and Exploration Institute (LNYS202101), and the Key Laboratory of Gold Mineralization Processes and Resource Utilization Subordinated to the Ministry of Natural Resources and the Key Laboratory of Metallogenic Geological Process and Resources Utilization in Shandong Province (KFKT201802, KFKT202102).

Data Availability Statement: All the data is presented in the paper.

Conflicts of Interest: The authors declare no conflict of interest.

References

1. Wu, Y.B.; Hanchar, J.M.; Gao, S.; Sylvester, P.J.; Tubrett, M.; Qiu, H.N.; Wijbrans, J.R.; Brouwer, F.M.; Yang, S.H.; Yang, Q.J. Age and nature of eclogites in the Huwan shear zone, and the multi-stage evolution of the Qinling-Dabie-Sulu orogen, central China. *Earth Planet. Sci. Lett.* **2009**, *277*, 345–354. [[CrossRef](#)]
2. Wu, Y.B.; Zheng, Y.F. Tectonic evolution of a composite collision orogen: An overview on the Qinling-Tongbai-Hong'an-Dabie-Sulu orogenic belt in central China. *Gondwana Res.* **2013**, *23*, 1402–1428. [[CrossRef](#)]
3. Li, S.; Jahn, B.M.; Zhao, S.; Dai, L.; Li, X.; Suo, Y.; Guo, L.; Wang, Y.; Liu, X.; Lan, H. Triassic southeastward subduction of North China Block to South China Block: Insights from new geological, geophysical and geochemical data. *Earth-Sci. Rev.* **2017**, *166*, 270–285. [[CrossRef](#)]
4. Cho, M.; Kim, H. Metamorphic evolution of the Ogcheon belt, Korea: A review and new age constraints. *Int. Geol. Rev.* **2005**, *47*, 41–57. [[CrossRef](#)]
5. Li, S.; Kusky, T.M.; Zhao, G.; Liu, X.; Zhang, G.; Kopp, H.; Wang, L. Two-stage Triassic exhumation of HP-UHP terranes in the western Dabie orogen of China: Constraints from structural geology. *Tectonophysics* **2010**, *490*, 267–293. [[CrossRef](#)]
6. Li, S.; Zhao, G.; Zhang, G.; Liu, X.; Dong, S.; Wang, Y.; Liu, X.; Suo, Y.; Dai, L.; Jin, C. Not all folds and thrusts in the Yangtze foreland thrust belt are related to the Dabie Orogen: Insights from Mesozoic deformation south of the Yangtze River. *Geol. J.* **2010**, *45*, 650–663. [[CrossRef](#)]
7. Dong, Y.; Zhang, G.; Neubauer, F.; Liu, X.; Genser, J.; Hauzenberger, C. Tectonic evolution of the Qinling orogen, China: Review and synthesis. *J. Asian Earth Sci.* **2011**, *41*, 213–237. [[CrossRef](#)]
8. Dong, Y.; Zhang, G.; Hauzenberger, C.; Neubauer, F.; Yang, Z.; Liu, X. Palaeozoic tectonics and evolutionary history of the Qinling orogen: Evidence from geochemistry and geochronology of ophiolite and related volcanic rocks. *Lithos* **2011**, *122*, 39–56. [[CrossRef](#)]
9. Zheng, Y.F.; Zhang, L.; McClelland, W.C.; Cuthbert, S. Processes in continental collision zones: Preface. *Lithos* **2012**, *136*, 1–9. [[CrossRef](#)]
10. Qiu, K.F.; Yu, H.C.; Hetherington, C.; Huang, Y.Q.; Yang, T.; Deng, J. Tourmaline composition and boron isotope signature as a tracer of magmatic-hydrothermal processes. *Am. Mineral.* **2021**, *106*, 1033–1044. [[CrossRef](#)]
11. Hacker, B.R.; Ratschbacher, L.; Liou, J. Subduction, collision and exhumation in the ultrahigh-pressure Qinling-Dabie orogen. *Geol. Soc. Lond. Spec. Publ.* **2004**, *226*, 157–175. [[CrossRef](#)]
12. Hacker, B.R.; Wallis, S.R.; Ratschbacher, L.; Grove, M.; Gehrels, G. High-temperature geochronology constraints on the tectonic history and architecture of the ultrahigh-pressure Dabie-Sulu Orogen. *Tectonics* **2006**, *25*, TC5006. [[CrossRef](#)]
13. Ratschbacher, L.; Franz, L.; Enkelmann, E.; Jonckheere, R.; Pörschke, A.; Hacker, B.R.; Dong, S.; Zhang, Y. The Sino-Korean-Yangtze suture, the Huwan detachment, and the Paleozoic-Tertiary exhumation of (ultra) high-pressure rocks along the Tongbai-Xinxian-Dabie Mountains. *Spec. Pap. Geol. Soc. Am.* **2006**, *403*, 45.
14. Liu, X.; Wu, Y.; Gao, S.; Wang, J.; Peng, M.; Gong, H.; Liu, Y.; Yuan, H. Zircon U-Pb and Hf evidence for coupled subduction of oceanic and continental crust during the Carboniferous in the Huwan shear zone, western Dabie orogen, central China. *J. Metamorph. Geol.* **2011**, *29*, 233–249. [[CrossRef](#)]
15. Cheong, C.S.; Jeong, G.Y.; Kim, H.; Choi, M.S.; Lee, S.H.; Cho, M. Early Permian peak metamorphism recorded in U-Pb system of black slates from the Ogcheon metamorphic belt, South Korea, and its tectonic implication. *Chem. Geol.* **2003**, *193*, 81–92. [[CrossRef](#)]
16. Cho, M.; Kim, H.; Wan, Y.; Liu, D. U–Pb zircon ages of a granitic gneiss boulder in metadiamicite from the Ogcheon metamorphic belt, Korea. *Geosci. J.* **2004**, *8*, 355–362. [[CrossRef](#)]
17. Ernst, W.; Tsujimori, T.; Zhang, R.; Liou, J. Permo-Triassic collision, subduction-zone metamorphism, and tectonic exhumation along the East Asian continental margin. *Annu. Rev. Earth Planet. Sci.* **2007**, *35*, 73–110. [[CrossRef](#)]

18. Kim, H.S.; Ree, J.H.; Kim, J. Tectonometamorphic evolution of the Permo-Triassic Songrim (Indosinian) orogeny: Evidence from the late Paleozoic Pyeongan Supergroup in the northeastern Taebaeksan Basin, South Korea. *Int. J. Earth Sci.* **2012**, *101*, 483–498. [[CrossRef](#)]
19. Chamberlain, K.R.; Bowring, S.A. Apatite-feldspar U-Pb thermochronometer: A reliable, mid-range (~450 °C), diffusion-controlled system. *Chem. Geol.* **2001**, *172*, 173–200. [[CrossRef](#)]
20. Schoene, B.; Bowring, S.A. Determining accurate temperature-time paths from U-Pb thermochronology: An example from the Kaapvaal craton, southern Africa. *Geochim. Cosmochim. Acta* **2007**, *71*, 165–185. [[CrossRef](#)]
21. Chew, D.M.; Sylvester, P.J.; Tubrett, M.N. U-Pb and Th-Pb dating of apatite by LA-ICPMS. *Chem. Geol.* **2011**, *280*, 200–216. [[CrossRef](#)]
22. Kirkland, C.; Yakymchuk, C.; Szilas, K.; Evans, N.; Hollis, J.; McDonald, B.; Gardiner, N. Apatite: A U-Pb thermochronometer or geochronometer? *Lithos* **2018**, *318*, 143–157. [[CrossRef](#)]
23. Yu, H.C.; Qiu, K.F.; Hetherington, C.J.; Chew, D.; Huang, Y.Q.; He, D.Y.; Geng, J.Z.; Xian, H.Y. Apatite as an alternative petrochronometer to trace the evolution of magmatic systems containing metamict zircon. *Contrib. Mineral. Petrol.* **2021**, *176*, 23. [[CrossRef](#)]
24. Yu, H.C.; Qiu, K.F.; Chew, D.; Yu, C.; Ding, Z.J.; Zhou, T.; Li, S.; Sun, K.F. Buried Triassic rocks and vertical distribution of ores in the giant Jiaodong gold province (China) revealed by apatite xenocrysts in hydrothermal quartz veins. *Ore Geol. Rev.* **2022**, *140*, 104612. [[CrossRef](#)]
25. Hu, L.; Li, Y.K.; Wu, Z.J.; Bai, Y.; Wang, A.J. Two metasomatic events recorded in apatite from the ore-hosting dolomite marble and implications for genesis of the giant Bayan Obo REE deposit, Inner Mongolia, Northern China. *J. Asian Earth Sci.* **2019**, *172*, 56–65. [[CrossRef](#)]
26. Kerrich, R.; Cassidy, K.F. Temporal relationships of lode gold mineralization to accretion, magmatism, metamorphism and deformation—Archean to present: A review. *Ore Geol. Rev.* **1994**, *9*, 263–310. [[CrossRef](#)]
27. Chesley, J.T.; Rudnick, R.L.; Lee, C.T. Re-Os systematics of mantle xenoliths from the East African Rift: Age, structure, and history of the Tanzanian craton. *Geochim. Cosmochim. Acta* **1999**, *63*, 1203–1217. [[CrossRef](#)]
28. Harlov, D.E. Apatite: A fingerprint for metasomatic processes. *Elements* **2015**, *11*, 171–176. [[CrossRef](#)]
29. Chew, D.M.; Spikings, R.A. Geochronology and thermochronology using apatite: Time and temperature, lower crust to surface. *Elements* **2015**, *11*, 189–194. [[CrossRef](#)]
30. Zeng, L.P.; Zhao, X.F.; Li, X.C.; Hu, H.; McFarlane, C. In situ elemental and isotopic analysis of fluorapatite from the Taocun magnetite-apatite deposit, Eastern China: Constraints on fluid metasomatism. *Am. Mineral.* **2016**, *101*, 2468–2483. [[CrossRef](#)]
31. Qiu, Y.; Groves, D.I.; McNaughton, N.J.; Wang, L.G.; Zhou, T. Nature, age, and tectonic setting of granitoid-hosted, orogenic gold deposits of the Jiaodong Peninsula, eastern North China craton, China. *Miner. Depos.* **2002**, *37*, 283–305. [[CrossRef](#)]
32. Mills, S.E.; Tomkins, A.G.; Weinberg, R.F.; Fan, H.R. Implications of pyrite geochemistry for gold mineralisation and remobilisation in the Jiaodong gold district, northeast China. *Ore Geol. Rev.* **2015**, *71*, 150–168. [[CrossRef](#)]
33. Deng, J.; Wang, Q.; Santosh, M.; Liu, X.; Liang, Y.; Yang, L.; Zhao, R.; Yang, L. Remobilization of metasomatized mantle lithosphere: A new model for the Jiaodong gold province, eastern China. *Miner. Depos.* **2020**, *55*, 257–274. [[CrossRef](#)]
34. Qiu, K.F.; Goldfarb, R.J.; Deng, J.; Yu, H.; Gou, Z.; Ding, Z.; Wang, Z.; Li, D. Gold deposits of the Jiaodong Peninsula, eastern China. *SEG Spec. Publ.* **2020**, *23*, 753–773.
35. Deng, J.; Yang, L.Q.; Li, R.H.; Groves, D.I.; Santosh, M.; Wang, Z.L.; Sai, S.X.; Wang, S.R. Regional structural control on the distribution of world-class gold deposits: An overview from the Giant Jiaodong Gold Province, China. *Geol. J.* **2019**, *54*, 378–391. [[CrossRef](#)]
36. Deng, J.; Wang, Q.F.; Yang, L.Q.; Zhou, L.; Gong, Q.J.; Yuan, W.M.; Xu, H.; Guo, C.Y.; Liu, X.W. The structure of ore-controlling strain and stress fields in the Shangzhuang gold deposit in Shandong province, China. *Acta Geol. Sin.-Engl. Ed.* **2008**, *82*, 769–780.
37. Deng, J.; Wang, C.; Bagas, L.; Carranza, E.J.M.; Lu, Y. Cretaceous-Cenozoic tectonic history of the Jiaojia Fault and gold mineralization in the Jiaodong Peninsula, China: Constraints from zircon U-Pb, illite K-Ar, and apatite fission track thermochronometry. *Miner. Depos.* **2015**, *50*, 987–1006. [[CrossRef](#)]
38. Deng, J.; Wang, C.; Bagas, L.; Santosh, M.; Yao, E. Crustal architecture and metallogenesis in the south-eastern North China Craton. *Earth-Sci. Rev.* **2018**, *182*, 251–272. [[CrossRef](#)]
39. Dou, J.Z.; Zhang, H.F.; Tong, Y.; Wang, F.; Chen, F.K.; Li, S.R. Application of geothermo-barometers to Mesozoic granitoids in the Jiaodong Peninsula, eastern China: Criteria for selecting methods of pressure estimation and implications for crustal exhumation. *J. Asian Earth Sci.* **2018**, *160*, 271–286. [[CrossRef](#)]
40. Liu, X.; Fan, H.R.; Evans, N.J.; Yang, K.F.; Danišik, M.; McInnes, B.I.; Qin, K.Z.; Yu, X.F. Exhumation history of the Sanshandao Au deposit, Jiaodong: Constraints from structural analysis and (U-Th)/He thermochronology. *Sci. Rep.* **2017**, *7*, 7787. [[CrossRef](#)]
41. Wang, L.; Qiu, Y.; McNaughton, N.; Groves, D.; Luo, Z.; Huang, J.; Miao, L.; Liu, Y. Constraints on crustal evolution and gold metallogeny in the Northwestern Jiaodong Peninsula, China, from SHRIMP U-Pb zircon studies of granitoids. *Ore Geol. Rev.* **1998**, *13*, 275–291. [[CrossRef](#)]
42. Fan, H.R.; Zhai, M.G.; Xie, Y.H.; Yang, J.H. Ore-forming fluids associated with granite-hosted gold mineralization at the Sanshandao deposit, Jiaodong gold province, China. *Miner. Depos.* **2003**, *38*, 739–750. [[CrossRef](#)]
43. Goldfarb, R.; Qiu, K.F.; Deng, J.; Chen, Y.; Yang, L. Orogenic gold deposits of China. *SEG Spec. Publ.* **2019**, *22*, 263–324.

44. Zhao, Z.F.; Zheng, Y.F.; Zhang, J.; Dai, L.Q.; Li, Q.; Liu, X. Syn-exhumation magmatism during continental collision: Evidence from alkaline intrusives of Triassic age in the Sulu orogen. *Chem. Geol.* **2012**, *328*, 70–88. [\[CrossRef\]](#)
45. Deng, J.; Qiu, K.F.; Wang, Q.F.; Goldfarb, R.; Yang, L.Q.; Zi, J.W.; Geng, J.Z.; Ma, Y. In situ dating of hydrothermal monazite and implications for the geodynamic controls on ore formation in the Jiaodong gold province, eastern China. *Econ. Geol.* **2020**, *115*, 671–685. [\[CrossRef\]](#)
46. Song, M.; Yang, L.; Fan, H.; Yu, X.; Ding, Z.; Zhang, Y.; Qiu, K.; Li, J.; Zhang, L.; Wang, B. Current progress of metallogenic research and deep prospecting of gold deposits in the Jiaodong Peninsula during 10 years for Exploration Breakthrough Strategic Action. *Geol. Bull. China* **2022**, *41*, 903–935.
47. Yang, L.; Wei, Y.; Wang, S.; Zhang, L.; Ju, L.; Li, R.; Gao, X.; Qiu, K. A preliminary study of reserve estimate and resource potential assessment of critical elements in the Jiaodong gold deposits, China. *Acta Petrol. Sin.* **2022**, *38*, 9–22.
48. Deng, J.; Yang, L.Q.; Groves, D.I.; Zhang, L.; Qiu, K.F.; Wang, Q.F. An integrated mineral system model for the gold deposits of the giant Jiaodong province, eastern China. *Earth-Sci. Rev.* **2020**, *208*, 103274. [\[CrossRef\]](#)
49. Sai, S.X.; Deng, J.; Qiu, K.F.; Miggins, D.P.; Zhang, L. Textures of auriferous quartz-sulfide veins and $^{40}\text{Ar}/^{39}\text{Ar}$ geochronology of the Rushan gold deposit: Implications for processes of ore-fluid infiltration in the eastern Jiaodong gold province, China. *Ore Geol. Rev.* **2020**, *117*, 103254. [\[CrossRef\]](#)
50. Yu, H.C.; Qiu, K.F.; Deng, J.; Zhu, R.; Mathieu, L.; Sai, S.X.; Sha, W.J. Exhuming and preserving epizonal orogenic Au-Sb deposits in rapidly uplifting orogenic settings. *Tectonics* **2022**, *41*, e2021TC007165. [\[CrossRef\]](#)
51. Zhao, G.; Zhai, M. Lithotectonic elements of Precambrian basement in the North China Craton: Review and tectonic implications. *Gondwana Res.* **2013**, *23*, 1207–1240. [\[CrossRef\]](#)
52. He, D.Y.; Qiu, K.F.; Yu, H.C.; Huang, Y.Q.; Ding, Z.J.; Shen, Y. Petrogenesis of the Early Cretaceous trachy-dacite from Mashan in the Jiaolai Basin, North China Craton. *Acta Petrol. Sin.* **2020**, *36*, 3705–3720.
53. Yang, K.F.; Fan, H.R.; Santosh, M.; Hu, F.F.; Wilde, S.A.; Lan, T.G.; Lu, L.N.; Liu, Y.S. Reactivation of the Archean lower crust: Implications for zircon geochronology, elemental and Sr-Nd-Hf isotopic geochemistry of late Mesozoic granitoids from northwestern Jiaodong Terrane, the North China Craton. *Lithos* **2012**, *146*, 112–127. [\[CrossRef\]](#)
54. Wei, Y.J.; Yang, L.; Qiu, K.F.; Wang, S.; Ren, F.; Dai, Z.; Li, D.; Shan, W.; Li, Z.; Wang, J. Geology, mineralogy and pyrite trace elements constraints on gold mineralization mechanism at the giant Dayingezhuang gold deposit, Jiaodong Peninsula, China. *Ore Geol. Rev.* **2022**, *148*, 104992. [\[CrossRef\]](#)
55. Song, M.C.; Lin, S.Y.; Yang, L.Q.; Song, Y.; Ding, Z.; Li, J.; Li, S.; Zhou, M. Metallogenic model of Jiaodong Peninsula gold deposits. *Miner. Depos.* **2020**, *39*, 215–236.
56. Goldfarb, R.J.; Mao, J.W.; Qiu, K.F.; Goryachev, N. The great Yanshanian metallogenic event of eastern Asia: Consequences from one hundred million years of plate margin geodynamics. *Gondwana Res.* **2021**, *100*, 223–250. [\[CrossRef\]](#)
57. Long, Z.Y.; Qiu, K.F.; Santosh, M.; Yu, H.C.; Jiang, X.Y.; Zou, L.Q.; Tang, D.W. Fingerprinting the metal source and cycling of the world's largest antimony deposit in Xikuangshan, China. *Geol. Soc. Am. Bull.* **2022**. *online*. [\[CrossRef\]](#)
58. Cochrane, R.; Spikings, R.A.; Chew, D.; Wotzlaw, J.F.; Chiaradia, M.; Tyrrell, S.; Schaltegger, U.; Van der Lelij, R. High temperature (>350 °C) thermochronology and mechanisms of Pb loss in apatite. *Geochim. Cosmochim. Acta* **2014**, *127*, 39–56. [\[CrossRef\]](#)
59. Schoene, B.; Bowring, S.A. U-Pb systematics of the McClure Mountain syenite: Thermochronological constraints on the age of the 40 Ar/39 Ar standard MMhb. *Contrib. Mineral. Petrol.* **2006**, *151*, 615. [\[CrossRef\]](#)
60. McDowell, F.W.; McIntosh, W.C.; Farley, K.A. A precise 40Ar-39Ar reference age for the Durango apatite (U-Th)/He and fission-track dating standard. *Chem. Geol.* **2005**, *214*, 249–263. [\[CrossRef\]](#)
61. Ludwig, K. ISOPLOT 3.00: A geochronological toolkit for Microsoft Excel (p. 39). *Berkeley Geochronol. Cent. Spec. Publ.* **2003**, *4*, 70.
62. Liu, Y.; Gao, S.; Hu, Z.; Gao, C.; Zong, K.; Wang, D. Continental and oceanic crust recycling-induced melt-peridotite interactions in the Trans-North China Orogen: U-Pb dating, Hf isotopes and trace elements in zircons from mantle xenoliths. *J. Petrol.* **2010**, *51*, 537–571. [\[CrossRef\]](#)
63. McDonough, W.F.; Sun, S.S. The composition of the Earth. *Chem. Geol.* **1995**, *120*, 223–253. [\[CrossRef\]](#)
64. Kusebauch, C.; John, T.; Whitehouse, M.J.; Klemme, S.; Putnis, A. Distribution of halogens between fluid and apatite during fluid-mediated replacement processes. *Geochim. Cosmochim. Acta* **2015**, *170*, 225–246. [\[CrossRef\]](#)
65. Sun, C.Y.; Cawood, P.A.; Xu, W.L.; Zhang, X.M.; Tang, J.; Li, Y.; Sun, Z.X.; Xu, T. In situ geochemical composition of apatite in granitoids from the eastern Central Asian Orogenic Belt: A window into petrogenesis. *Geochim. Cosmochim. Acta* **2021**, *317*, 552–573. [\[CrossRef\]](#)
66. O'Sullivan, G.; Chew, D.; Kenny, G.; Henrichs, I.; Mulligan, D. The trace element composition of apatite and its application to detrital provenance studies. *Earth-Sci. Rev.* **2020**, *201*, 103044. [\[CrossRef\]](#)
67. Belousova, E.; Walters, S.; Griffin, W.; O'reilly, S. Trace-element signatures of apatites in granitoids from the Mt Isa Inlier, northwestern Queensland. *Aust. J. Earth Sci.* **2001**, *48*, 603–619. [\[CrossRef\]](#)
68. Li, Z.; Duan, D.; Jiang, S.; Ma, Y.; Yuan, H. In situ analysis of major elements, trace elements and Sr isotopic compositions of apatite from the granite in the Chengchao skarn-type Fe deposit, Edong ore district: Implications for petrogenesis and mineralization. *J. Earth Sci.* **2018**, *29*, 295–306. [\[CrossRef\]](#)
69. Harlov, D.E.; Förster, H.-J. Fluid-induced nucleation of (Y+REE)-phosphate minerals within apatite: Nature and experiment. Part II. Fluorapatite. *Am. Mineral.* **2003**, *88*, 1209–1229. [\[CrossRef\]](#)
70. Barth, T.F. The feldspar geologic thermometers. *Neues Jahrb. Für Mineral.* **1951**, *82*, 143–154.

71. Qiu, K.F.; Yu, H.C.; Gou, Z.Y.; Liang, Z.L.; Zhang, J.L.; Zhu, R. Nature and origin of Triassic igneous activity in the Western Qinling Orogen: The Wenquan composite pluton example. *Int. Geol. Rev.* **2018**, *60*, 242–266. [[CrossRef](#)]
72. Streck, M.J. Mineral textures and zoning as evidence for open system processes. *Rev. Mineral. Geochem.* **2008**, *69*, 595–622. [[CrossRef](#)]
73. Ladenburger, S.; Marks, M.A.; Upton, B.; Hill, P.; Wenzel, T.; Markl, G. Compositional variation of apatite from rift-related alkaline igneous rocks of the Gardar Province, South Greenland. *Am. Mineral.* **2016**, *101*, 612–626. [[CrossRef](#)]
74. Gao, Y.J.; Zhang, Y.M.; Yan, P.K. Study of ore-controlling conditions and ore-forming type of Tudui gold deposit in Haiyang Shandong. *J. Liaoning Univ. Technol.* **2006**, *26*, 239–242.
75. Feng, B.; Li, H.M.; Wei, M.L.; Tao, X.; Zhang, W.S. Chronological study on Muniushan pluton in Guocheng District of Jiaodong Peninsula and its geological significance. *Gold* **2013**, *34*, 24–28.
76. Xu, H.; Wang, L.; Chen, C.; Wang, X.; Liu, J.; Wu, Q. Condition of geochemistry and zircon U-Pb geochronology for monzonitic granite in Muniushan, Guocheng, Shandong. *Glob. Geol.* **2015**, *34*, 927–937.
77. Cheng, S.B.; Liu, Z.J.; Wang, Q.F.; Feng, B.; Wei, X.L.; Liu, B.Z.; Qin, L.Y.; Zhao, B.J.; Shui, P.; Xu, L. SHRIMP zircon U-Pb dating and Hf isotope analyses of the Muniushan Monzogranite, Guocheng, Jiaobei Terrane, China: Implications for the tectonic evolution of the Jiao-Liao-Ji Belt, North China Craton. *Precamb. Res.* **2017**, *301*, 36–48. [[CrossRef](#)]
78. Zhang, L.; Chen, Z.; Wang, F.; Zhou, T. Apatite geochemistry as an indicator of petrogenesis and uranium fertility of granites: A case study from the Zhuguangshan batholith, South China. *Ore Geol. Rev.* **2020**, *128*, 103886. [[CrossRef](#)]
79. Maruyama, S.; Liou, J.; Terabayashi, M. Blueschists and eclogites of the world and their exhumation. *Int. Geol. Rev.* **1996**, *38*, 485–594. [[CrossRef](#)]
80. Brown, M. Metamorphic conditions in orogenic belts: A record of secular change. *Int. Geol. Rev.* **2007**, *49*, 193–234. [[CrossRef](#)]
81. Miyashiro, A. Evolution of metamorphic belts. *J. Petrol.* **1961**, *2*, 277–311. [[CrossRef](#)]
82. Miyashiro, A. Paired and unpaired metamorphic belts. *Tectonophysics* **1973**, *17*, 241–254. [[CrossRef](#)]
83. Zhou, T.; Qiu, K.F.; Wang, Y.; Yu, H.C.; Hou, Z.L. Apatite Eu/ Y-Ce discrimination diagram: A big data based approach for provenance classification. *Acta Petrol. Sin.* **2022**, *38*, 291–299.
84. Wang, Y.; Qiu, K.F.; Müller, A.; Hou, Z.L.; Zhu, Z.H.; Yu, H.C. Machine Learning Prediction of Quartz Forming-Environments. *J. Geophys. Res. Solid Earth* **2021**, *126*, e2021JB021925. [[CrossRef](#)]
85. Lai, S.; Qin, J. Zircon U-Pb dating and Hf isotopic composition of the diabase dike swarm from Sanchazi area, Mianlue suture: Chronology evidence for the Paleo-Tethys oceanic crust subduction. *J. Earth Sci. Environ.* **2010**, *32*, 27–33.
86. Li, N.; Chen, Y.J.; Santosh, M.; Pirajno, F. Compositional polarity of Triassic granitoids in the Qinling Orogen, China: Implication for termination of the northernmost paleo-Tethys. *Gondwana Res.* **2015**, *27*, 244–257. [[CrossRef](#)]
87. Dai, L.Q.; Zheng, F.; Zhao, Z.F.; Zheng, Y.F. Recycling of Paleotethyan oceanic crust: Geochemical record from postcollisional mafic igneous rocks in the Tongbai-Hong’an orogens. *Bulletin* **2017**, *129*, 179–192. [[CrossRef](#)]
88. Wu, Y.B.; Gao, S.; Zhang, H.F.; Yang, S.H.; Jiao, W.F.; Liu, Y.S.; Yuan, H.L. Timing of UHP metamorphism in the Hong’an area, western Dabie Mountains, China: Evidence from zircon U-Pb age, trace element and Hf isotope composition. *Contrib. Mineral. Petrol.* **2008**, *155*, 123–133. [[CrossRef](#)]
89. Cheng, H.; Vervoort, J.D.; Dragovic, B.; Wilford, D.; Zhang, L. Coupled Lu-Hf and Sm-Nd geochronology on a single eclogitic garnet from the Huwan shear zone, China. *Chem. Geol.* **2018**, *476*, 208–222. [[CrossRef](#)]
90. Zhou, L.G.; Xia, Q.X.; Zheng, Y.F.; Chen, R.X.; Hu, Z.; Yang, Y. Tectonic evolution from oceanic subduction to continental collision during the closure of Paleotethyan ocean: Geochronological and geochemical constraints from metamorphic rocks in the Hong’an orogen. *Gondwana Res.* **2015**, *28*, 348–370. [[CrossRef](#)]
91. Liu, X.; Li, S.; Jahn, B.M. Tectonic evolution of the Tongbai-Hong’an orogen in central China: From oceanic subduction/accretion to continent-continent collision. *Sci. China Earth Sci.* **2015**, *58*, 1477–1496. [[CrossRef](#)]
92. Oh, C.W.; Lee, B.C. The relationship between systematic metamorphic patterns and collisional processes along the Qinling-Sulu-Odesan collisional belt between the North and South China Cratons. *Geo. Soc. Lond. Spec. Pub.* **2019**, *478*, 449–475. [[CrossRef](#)]
93. Yu, H.C.; Qiu, K.F.; Pirajno, F.; Zhang, P.C.; Dong, W.Q. Revisiting Phanerozoic evolution of the Qinling Orogen (East Tethys) with perspectives of detrital zircon. *Gondwana Res.* **2022**, *103*, 426–444. [[CrossRef](#)]
94. Cheng, H.; King, R.L.; Nakamura, E.; Vervoort, J.D.; Zheng, Y.F.; Ota, T.; Wu, Y.B.; Kobayashi, K.; Zhou, Z.Y. Transitional time of oceanic to continental subduction in the Dabie orogen: Constraints from U-Pb, Lu-Hf, Sm-Nd and Ar-Ar multichronometric dating. *Lithos* **2009**, *110*, 327–342. [[CrossRef](#)]
95. Cheng, H.; DuFrane, S.A.; Vervoort, J.D.; Nakamura, E.; Zheng, Y.F.; Zhou, Z. Protracted oceanic subduction prior to continental subduction: New Lu-Hf and Sm-Nd geochronology of oceanic-type high-pressure eclogite in the western Dabie orogen. *Am. Mineral.* **2010**, *95*, 1214–1223. [[CrossRef](#)]
96. Fu, B.; Zheng, Y.F.; Touret, J.L. Petrological, isotopic and fluid inclusion studies of eclogites from Sujiahe, NW Dabie Shan (China). *Chem. Geol.* **2002**, *187*, 107–128. [[CrossRef](#)]
97. Sun, W.; Williams, I.; Li, S. Carboniferous and Triassic eclogites in the western Dabie Mountains, east-central China: Evidence for protracted convergence of the North and South China blocks. *J. Metamorph. Geol.* **2002**, *20*, 873–886. [[CrossRef](#)]
98. Liu, X.; Jahn, B.M.; Liu, D.; Dong, S.; Li, S. SHRIMP U-Pb zircon dating of a metagabbro and eclogites from western Dabieshan (Hong’an Block), China, and its tectonic implications. *Tectonophysics* **2004**, *394*, 171–192. [[CrossRef](#)]

99. Jahn, B.M.; Liu, X.; Yui, T.F.; Morin, N.; Coz, M. High-pressure/ultrahigh-pressure eclogites from the Hong'an Block, East-Central China: Geochemical characterization, isotope disequilibrium and geochronological controversy. *Contrib. Mineral. Petrol.* **2005**, *149*, 499–526. [[CrossRef](#)]
100. Peters, T.J.; Ayers, J.C.; Gao, S.; Liu, X.M. The origin and response of zircon in eclogite to metamorphism during the multi-stage evolution of the Huwan Shear Zone, China: Insights from Lu-Hf and U-Pb isotopic and trace element geochemistry. *Gondwana Res.* **2013**, *23*, 726–747. [[CrossRef](#)]
101. Cho, D.L.; Lee, S.R.; Armstrong, R. Termination of the Permo-Triassic Songrim (Indosinian) orogeny in the Ogcheon belt, South Korea: Occurrence of ca. 220 Ma post-orogenic alkali granites and their tectonic implications. *Lithos* **2008**, *105*, 191–200. [[CrossRef](#)]
102. Zhang, L.X.; Liu, P.H.; Wang, Y.L.; Zhou, W.P.; Zhang, Y.J.; Zhang, C.H. Depositional timing and provenance characteristics of the Cretaceous insishan formation in the Shewopo Area, Jiaolai Basin: New evidence from Detrital Zircon U-Pb dating and REE composition. *Earth Sci.* **2021**, *46*, 1119–1132.
103. Peng, N.; Liu, Y.Q.; Kuang, H.W.; Xu, H.; Zhang, P.; Chen, J.; An, W.; Wang, N.S. Provenance of early cretaceous Laiyang group in Jiaolai basin and its significance. *Geol. China* **2015**, *42*, 1793–1810.
104. Zhang, P.; Kuang, H.W.; Liu, Y.Q.; Peng, N.; Xu, H.; Wang, M.W.; An, W.; Wang, N.S. Conglomerates on the base Linsishan Formation of the middle early cretaceous in Jiaolai Basin of eastern Shandong, and implications for basin evolution. *Acta Sedimentol. Sin.* **2016**, *34*, 15–32.